Characterisation and properties of powder-rolled porous Ti sheets and Ti/IrO_2 electrodes

Gang Chen[1]*, G.Z. Li[1], C.S. Xiang[2], S.Y. Zhao[1], P. Tan[1], H.P. Tang[1]*, Peng Cao[3]

[1]State Key Laboratory of Porous Metal Materials, Northwest Institute for Nonferrous Metal Research, Xi'an, Shaanxi, 710016, P.R. China

[2]Xi'an Sailong Metal Materials Co. Ltd., Xi'an, Shaanxi, 710016, P.R. China

[3]Department of Chemical and Materials Engineering, The University of Auckland, Private Bag 92019, Auckland 1142, New Zealand

*Corresponding author. Tel.: +86-29-86231095; Fax: +86-29-86264926.

Email addresses: mychgcsu@163.com (G. Chen); hptang@c-nin.com (H.P. Tang).

Abstract

This report investigated synthesis of porous titanium (Ti) sheets by direct powder rolling followed by vacuum sintering at 1100 ℃ for 1.5 h. Uniform microstructures were observed on the sections longitudinal and transverse to rolling direction (RD) in terms of porosity and pore size. The as-sintered porous Ti sheet was also used as an electrode substrate and IrO_2 nanowire arrays were coated onto the substrate by thermal decomposition. Characterisation results show that the coating mainly exhibited mixture of IrO_2 and α-Ti phases. The IrO_2 nanowire arrays coating effectively increased the specific surface area of the Ti/IrO_2 electrode. The cyclic voltammetry test for the Ti/IrO_2 electrode obtained an obvious redox peak. This electrode with IrO_2 nanowire arrays reached over 95% of current efficiency.

Keywords: Titanium; Porous; Powder rolling; Coating, Electrochemical property

1. Introduction

Porous titanium (Ti) has a low density, excellent corrosion resistance, sound mechanical properties and outstanding biocompatibility [1]. It has been attracting attention in multiple fields such as aerospace or submarine vehicles, electrode plates, medical devices, and industrial filters [2-6]. In comparison to conventional press-and-sinter, direct powder rolling has been become the most attractive powder metallurgical method to produce large-scale thin metal sheets/foils/plates [7-9].

Powder rolling of common engineering materials has been practiced since 1909 [10], while the first report on powder rolling of Ti sheets was published in 1953 [11]. Since then, studies of the Ti sheets and plates by powder rolling followed suit. In particular, large-scale porous Ti sheets are increasingly used as electrode plates in the electrocatalytic applications [12]. They are also used in filtration devices in food industry, e.g., wine and fruit juice processing [13]. Due to its industrial significance, it is important to investigate the properties of filtration and electrocatalysis associated with porous Ti sheets. There have been many investigations of Ti and its alloys sheets by powder rolling, e.g., pure Ti, Ti-6Al-4V, Ti-6Al-6V-2Sn, Ti-6Al-2Sn-4Zr-2Mo and γ-TiAl, with focus on the compaction theory, rolling parameters, sintering conditions, post-sintering treatments and microstructures [7, 8, 12, 14-20]. At present, Ti-supported IrO_2 electrodes are widely accepted in the electrolysis process, because they are more stable, have a longer life, exhibit excellent catalytic activity and do not cause contamination [21-24]. To our best knowledge, however, the reports on producing large-scale Ti sheets by powder rolling are limited and the use of large-scale Ti sheets as electrodes are scarce.

Thus, in this study we dealt with the manufacturing of large-scale porous Ti sheets by direct powder rolling followed by vacuum sintering. The resultant microstructure, tensile properties and filtration performance were reported. In addition, IrO_2 nanowire arrays were coated on the porous Ti sheet support, being used as an electrode. The electrocatalytic performance of the Ti-supported IrO_2 coating was also studied.

2. Experimental

2.1. Materials and powder rolling

Hydride-dehydride (HDH) Ti powders supplied by Xi'an Baode Co. Ltd., which have a medium particle size of 50 μm, apparent density of 1.54 g/cm^3 and oxygen content of 0.28 wt.%, were used in this study as shown in Fig. 1(a). With a close control of rolling parameters, the powder feeding rate, rolling speed, roll diameter and rolling load were set at 50 g/s, 1 m/min, 50 mm and 35 ton, respectively. Then, Ti powders were rolled into a sheet of 430 mm in width, 430 mm in length and 0.75 mm in thickness. The direct powder rolling is schematically presented in Fig. 1(b). The rolling compacted Ti sheet was then sintered in vacuum at 1100 ℃ for 1.5 h with a heating rate of 10 K/min (vacuum level: 10^{-3} Pa).

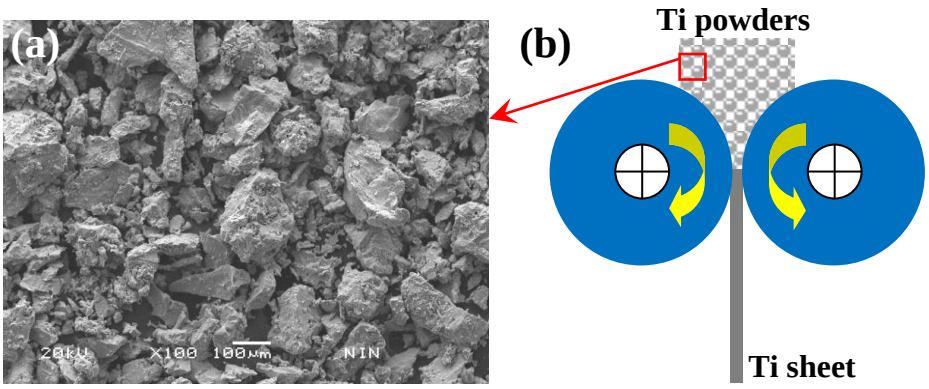

Fig. 1. (a) Micro morphology of the starting HDH-Ti powders for powder rolling and (b) schematic of the direct powder rolling procedure.

2.2. Microstructure characterisation and property measurement of the Ti sheet

Porosity of as-fabricated porous Ti sheets was measured by the Archimedes method as specified in the ASTM B962-14 standard. The pore size distribution, gas permeability and filtration flux tests were conducted using a pore-size distribution analyser (PSDA, TOPAS PSM165) using the bubble-point method as per the ASTM F316-03 standard. The filtration efficiency test was conducted on a gas/solid separation equipment (TOPAS AFC-131) running with ash, whose particle size ranges from 0.2 to 100.0 μm and concentration is below 5 g/Nm^3, according to the EN779-2002 standard. The samples (i.e., #1-2, 2-2 and 3-2 with a diameter of 30 mm in Fig. 2) were conducted both pore size and gas permeability analysis, while the other samples (i.e., #1-1, 2-1 and 3-1 with a diameter of 120 mm in Fig. 2) were performed filtration flux test. Only the sample (#2-1) did test the filtration efficiency. All the samples were cut from an identical sintered Ti sheet. To study the thickness homogeneity, the side-area thickness of the sheet before and after sintering was measured at an accuracy of 0.01 mm. The thickness measurement was performed at an interval of 10 mm either longitudinal or transverse to RD and thus totally 44 thickness data for each direction were investigated. Cross sections of the sintered Ti sheet were examined by an optical microscope (OM, Leica DM2500M). Surface and fractured cross-sectional morphologies of the Ti sheet and Ti/IrO_2 electrode were conducted using a scanning electron microscope (JEOL JSM-6700).

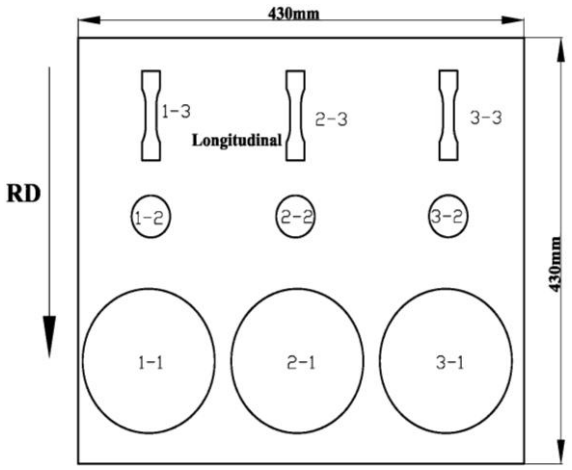

Fig. 2. Schematic of samples cut from the as-sintered Ti sheet.

2.3. IrO_2 coating preparation on the Ti substrate

The porous Ti/IrO_2 electrodes were fabricated by traditionally thermal decomposition of H_2IrCl_6 on the powder rolled porous substrate with a dimension of 2.0 cm×3.0 cm. To improve the cohesion between the substrate and coating, the porous Ti sheet was degreased and etched in boiling 10 % oxalic acid for *ca.* 10 min to remove surface oxides. The H_2IrCl_6 was dissolved in 1:1 (vol. %) butyl alcohol and isopropanol to prepare the precursor solution. Then, $TaCl_5$ solution was added in the precursor solution (Ir:Ta=7:3, at. %) to enhance its stability and reactivity of the coating. The metal concentration of the precursor solution is 0.2 mol/L. The precursors were brushed on the as-treated porous Ti sheet, dried at 50 ℃ for 10 min and calcinated at 500 ℃ in air for another 10 min [23]. The entire process was repeated until the precursors were consumed up, and the electrode was finally calcinated at 500 ℃ for 1 h [23], achieving a stable oxide layer. The final Ir content on the porous Ti support is 35g/m^2 in this study.

2.4. Microstructure and electrocatalytic properties of the IrO_2/Ti electrode

The as-sintered Ti sheet was cut into tensile bars (with a gage length of 20.0 mm) with an electric arc wire cutter. The longitudinal direction of the tensile bars is along rolling direction (RD), Fig. 2. The tensile properties of the as-cut Ti tensile bars were measured on an Instron 5967 universal machine with a cross-head speed of 0.5 mm/min at 25 ℃.

The working electrode was the IrO_2 coated porous Ti sheet (Ti/IrO_2) with an exposed area of 1 cm^2, while a graphite plate and a saturated calomel electrode (SCE) was used as the counter and reference electrode, respectively. The electrolyte solution was 0.5 M Na_2SO_4+0.05 M H_2SO_4. All chemicals were of reagent grade and all solutions were prepared by deionised (DI) water. Cyclic voltammetry was used to characterise the active surface of oxide electrodes at 28 ℃ using a ZHANER electrochemical workstation. Voltammetric curves were recorded between -0.3 and 1.3 V *vs.* SCE at a sweep rate (v) of 40 mV/s.

3. Results and discussion

3.1. Porous Ti sheet/substrate

3.1.1. Thickness homogeneity of the Ti sheet/substrate

Powder feeding is one of the most key techniques in powder rolling, which is normally dependent on the feeding mode [9, 25, 26]. Referring to the feeding mode, we designed a new feeding hopper to control the powder feeding that can effectively minimize load fluctuation and thus give rise to uniform thickness. In this case, the side-edge thickness either longitudinal or transverse to RD for the rolling compacted Ti sheet was measured at an interval of 10 mm and thus total 44 data for each direction were given in Fig. 3. As displayed in Fig. 3, the thicknesses of the side-edge Ti sheet longitudinal and transverse to RD range from 0.73 to 0.79 mm with a median size of 0.75 ± 0.02 and 0.75 ± 0.01 mm for the green state respectively (Fig. 3(a) and Fig. 3(b)), while both decreased after sintering but still with uniformity.

A pressure distribution exists between the roll surfaces during powder rolling. At large roll gaps insufficient pressure may be applied to the powders at a certain area of the sheet, and the thickness and porosity of the sheet at this point must therefore be lower than those at other points [27]. However, it can be concluded that both the thickness and porosity varieties (Fig. 3 and Table 1) in either longitudinal or transverse to RD seem negligible, although it is believed such difference is arising from the inconsistent roll gap and powder feeding rate during rolling.

It needs to point that the thickness-homogeneity control is a widely-known world puzzle for large-scale metal sheets by direct powder rolling. Nevertheless, this

problem has been successfully settled with achieving sound thickness homogeneity for the large-scale Ti sheet in our study.

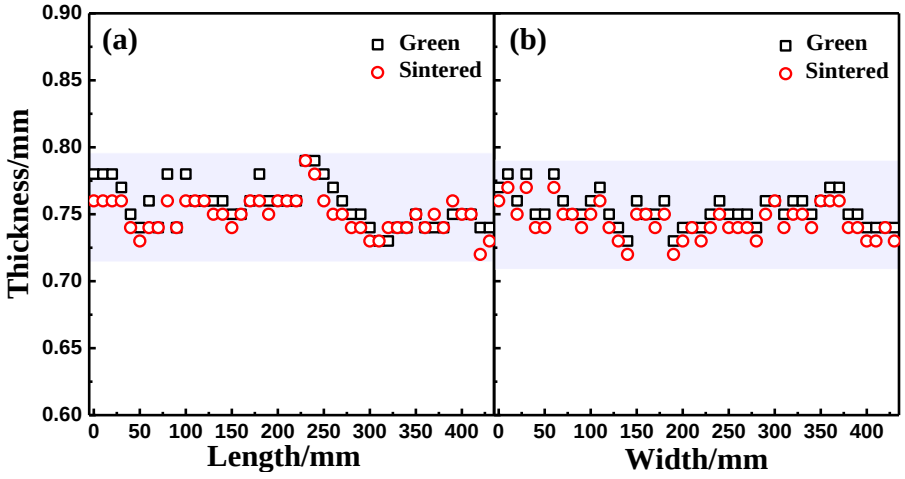

Fig. 3. Side-edge thickness of the Ti sheet before and after sintering (a) longitudinal and (b) transverse to RD.

3.1.2. Microstructure of the Ti sheet/substrate

Fig. 4 illustrates macroscopic and microscopic images of both green and as-sintered Ti sheets that cannot be observed any distortion or surface cracks, Figs. 4(a) and 4(c). As can be seen in Fig. 4(b), some green particles were compressed and thus seem elongated in RD after rolling, while there occurred sintering necking between particles after sintering (Fig. 4(d)). This is because metal particles were first pressed into intimate contact and then, if the pressure is sufficiently high, elongated in RD [15, 27, 28]. The degree of elongation depends on both the pressure and the ductility of the metal [15, 27, 28]. In this case, successive cold rolling steps may lead to deformation of particles in RD, and the particles were elongated with cold working as shown in Figs. 4 and 5.

Fig. 5 compares the OM micrographs of both surface and cross-sectional microstructure in the green-state and as-sintered porous Ti sheets. It can be seen from Fig. 5(a) that the pores are larger in the green state than those in the sintered sample (Fig. 5(c)). This is simply due to the sintering necking formed after high temperature solid-state sintering and thus densification, resulting in shrinkage of pores in the sintered sample [29]. This also yields the thickness shrinkage after sintering (Fig. 3). Furthermore, most pores are interconnected and irregular in the either green or

sintered sample. It is noteworthy that there are a good deal of inner micro-pores in the original particles as shown in Fig. 5(a) and most of these micro-pores retained after high temperature sintering (Fig. 5(c)). On the other hand, the original pores, namely the interspacing among Ti particles after rolling, shrank after high-temperature sintering, Fig. 4(d) *cf.* Fig. 4(b) [29]. Therefore, both types of pore are contributable to the final total porosity as presented in Table 1.

The pore size distribution analysis was performed using all the #X-2 samples while their results are similar. Thus, we only chose the result from the #2-2 sample as an example shown in Fig. 6. It can be seen from Fig. 6 that its pore size is mainly in the range between 6.0 and 7.5 μm, and the maximum pore size is below 13.0 μm. As summarized in Table 1, although the total porosity and mean pore size are slightly different among the three samples (i.e., #1-2, 2-2 and 3-2), they are fairly resemble. This indicates that we achieved Ti sheets with microstructural homogeneity transverse to RD.

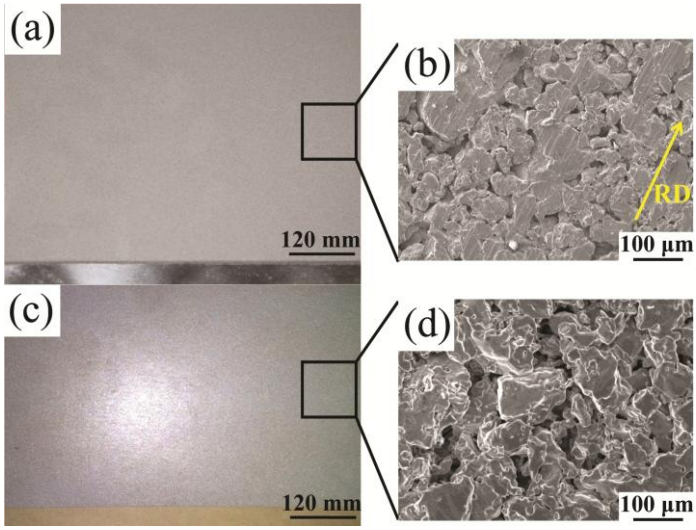

Fig. 4. Images of the green-state Ti sheet before sintering (a) macroscopic and (b) microscopic; as-sintered state after sintering (c) macroscopic and (d) microscopic.

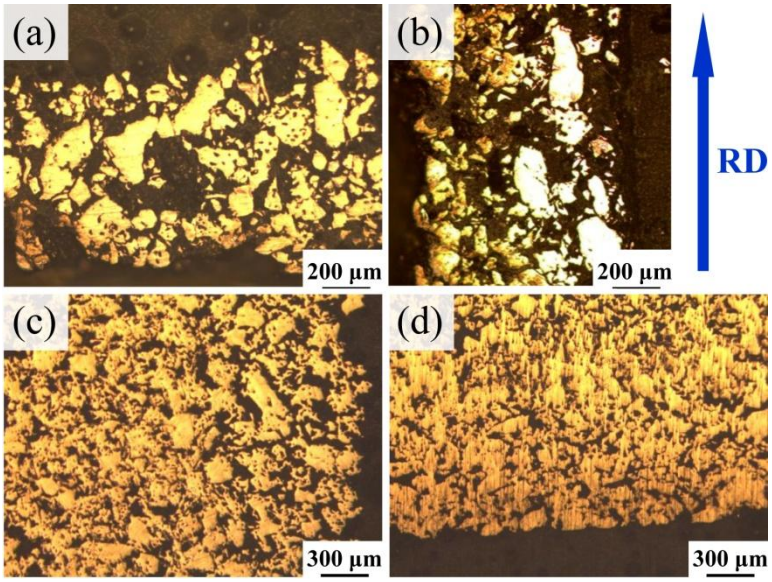

Fig. 5. Microscopic images observed from the green-state Ti sheet (a) surface and (b) cross section; the as-sintered Ti sheet (c) surface and (d) cross section.

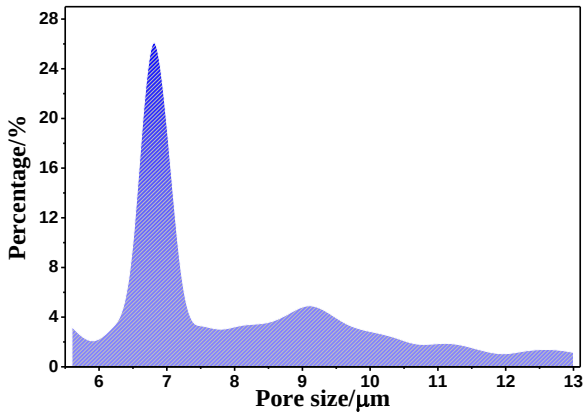

Fig. 6. Pore size distribution of the as-sintered #2-2 sample.

Table 1. Total porosity and mean pore size of the sintered samples.

Sample	Total porosity/%	Mean pore size/μm
#1-2	28.9±0.2	6.3±0.3
#2-2	28.1±0.4	5.9±0.2
#3-2	27.0±0.2	5.7±0.3

3.1.3. Tensile and filtration properties of the Ti sheet/substrate

As tabulated in Table 2, the tensile fracture strength of the #1-3, 2-3 and 3-3 samples longitudinal to RD is 97.1±4.1, 100.7±1.9 and 103.6±3.4 MPa, respectively. Moreover, the fracture strain of the three samples longitudinal to RD is *ca.* 1.83 %. We recall the porosity variation for the samples of #1-3, 2-3 and 3-3 (Table 1), which we believe is the cause to the difference of tensile fracture strength and strain. In spite of this, the difference of tensile properties among the three samples can be neglected.

Table 2. Static tensile properties of the sintered Ti sheets.

Sample	Fracture strength/MPa	Fracture strain/%
#1-3	97.1±4.1	1.83±0.03
#2-3	100.7±1.9	1.82±0.02
#3-3	103.6±3.4	1.83±0.05

Fig. 7 displays the linear curves of differential pressure *vs.* gas flow rate for the as-sintered #X-1 samples (i.e., #1-1, 2-1 and 3-1). As can be seen from Fig. 7, the differential pressure increases linearly with flow rate in all cases. Based on the P-Q curves, the calculated gas permeability is 195.3±13.3, 186.5±13.7 and 172.7±22.0 $m^3 \cdot m^{-2} \cdot kPa^{-1} \cdot h^{-1}$ for the #1-1, 2-1 and 3-1 samples, respectively. From a filtration engineering point of view, such difference of gas permeability is negligible although its value is the largest in the case of the #1-1 sample. This further implies the uniform filtration properties for the Ti sheet. Additionally, the sintered #2-1 sample performs high filtration efficiency (Fig. 8). It is interesting to note that the filtration efficiency increases significantly with ash particle size when it is below 0.5 μm. However, if the ash particle size arises above 0.5 μm, the filtration efficiency keeps a stable value, yielding up to 99 %. It is because there are limited micro-pores below 0.5 μm in the sintered sample so that ash with particle size below 0.5 μm cannot be intercepted by the pore channels. Therefore, with the increase of ash particle size, more ash particles are intercepted, thus achieving higher filtration efficiency (Fig. 8).

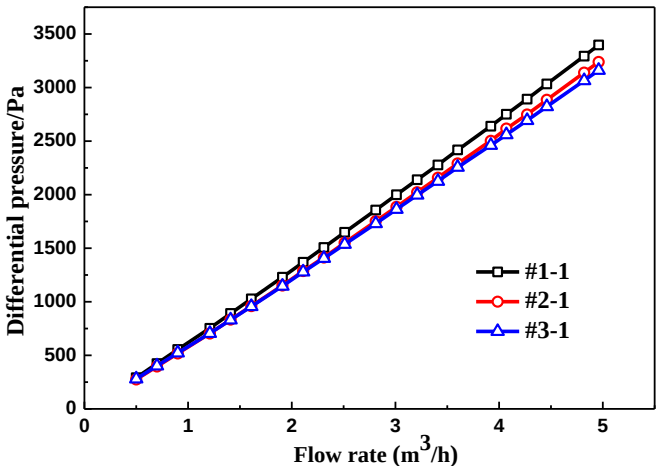

Fig. 7. The P-Q curves of the sintered #X-1 samples.

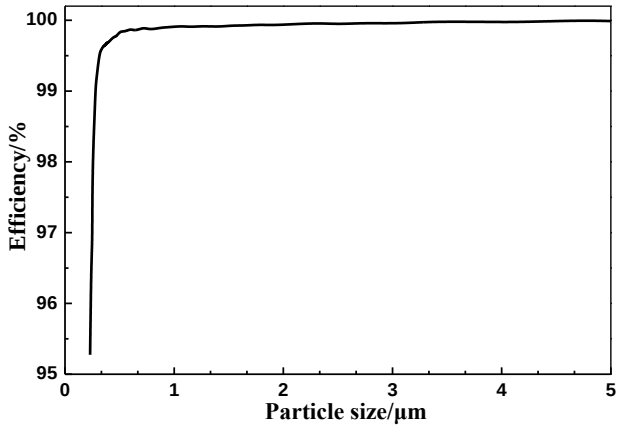

Fig. 8. The filtration efficiency of the sintered #2-1 sample.

3.2. Ti/IrO2 electrode

3.2.1. Microstructure of the IrO_2 coating

As mentioned previously, the brushing process was employed to prepare the IrO_2 coating on the porous Ti plate. Fig. 9 shows the SEM images of the Ti substrate before coating and either surface or cross section of the porous Ti/IrO_2 electrode, respectively. We can see from Figs. 9(b) and 9(e) that nanowire arrays were grown the Ti particles, forming a surface coating. In this case, the diameter of nanowires is *ca.* 50 nm. Due to the porous structure of the Ti plate, the specific surface area is large enough to accommodate the precursor solution. After being calcinated at 500 ℃ for 1 h, the precursor was rapidly decomposed and thus the coating was firmly adhered on the porous Ti substrate. The nanowire arrays were thought to increase the specific

surface areas of the porous electrode so that the reactivity of electrode would be also improved.

The XRD pattern for the IrO_2 coating is presented in Fig. 10. According to this pattern, the coating is consisted of IrO_2 and α-Ti phases. The α-Ti peak is coming from the substrate. It should be noted that because of thin thickness of the coating, the X ray penetrated into the substrate, which causes relatively strong Ti diffraction peak but weak IrO_2 peaks (Fig. 10).

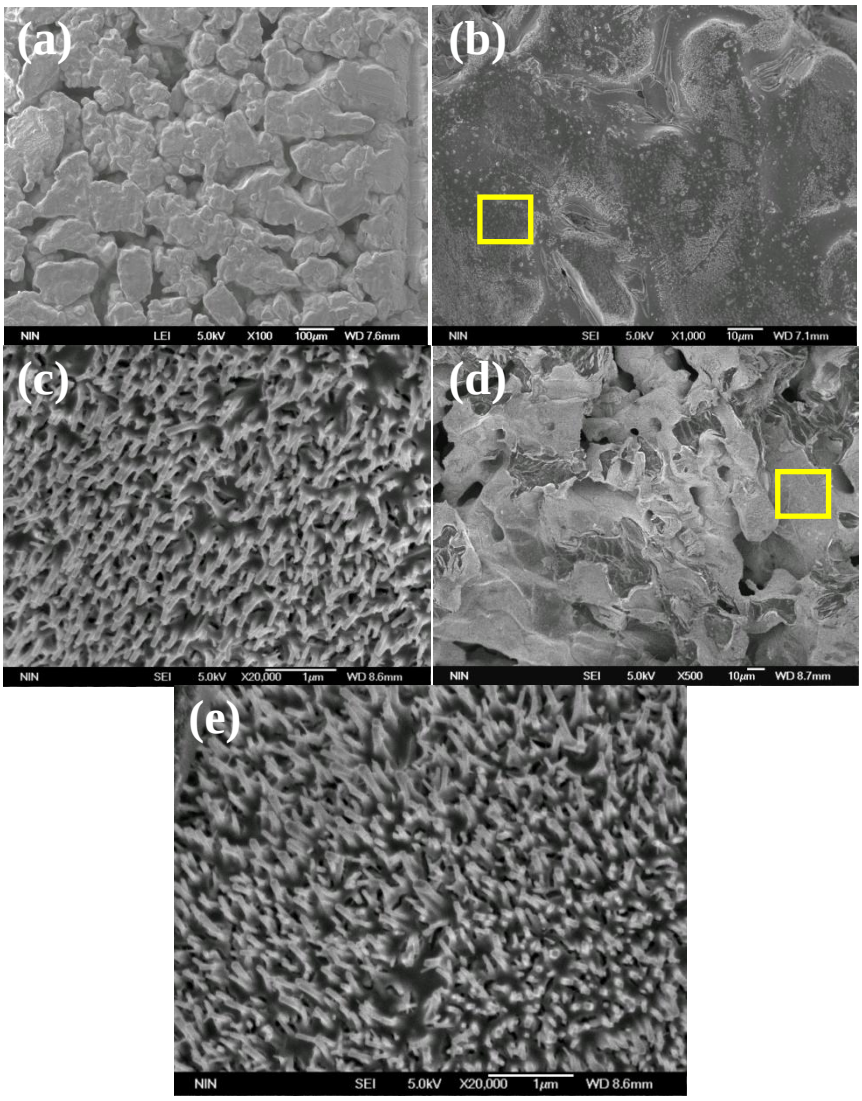

Fig. 9. SEM images of (a) the surface of the porous Ti substrate after etching, (b) the surface of the Ti/IrO_2 electrode after coating, (c) enlarged area in (b), (d) the fractured cross section of the Ti/IrO_2 electrode after coating and (e) enlarged area in (d).

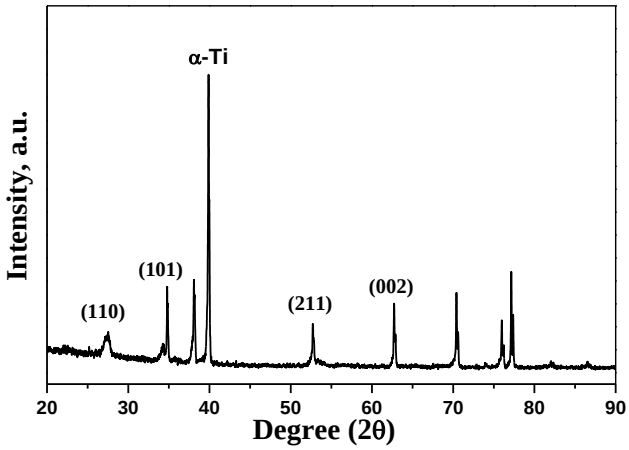

Fig. 10. The XRD pattern of the IrO_2 coating on the porous Ti substrate. All the reflections are indexed to IrO_2 phase except for the peak at ca. 40 degree being indexed to α-Ti.

3.2.2. Electrocatalytic properties of the IrO_2/Ti electrode

Fig. 11 shows the voltammetric curve of the IrO_2/Ti anode at 40 mV/s in the electrolyte solution. Y.Y. Hou et al. [23] tried a similar treatment to a densified Ti substrate and coated an IrO_2 layer on the Ti. Then, they finally calcinated the IrO_2/Ti electrode at 500 ℃ for 1 h. By comparing the corresponding voltammetric charge reported in Ref. [23], it shows our electrode coated on the porous Ti substrate achieved more active surface area than that coated on the densified Ti substrate in Ref. [23].

From Fig. 11 it can be seen an obvious current peak in the voltage range between 1.1 to 1.3 V *vs.* SCE. It implies the activity transformation occurred on the surface of the IrO_2/Ti anode. In other words, there is a transition from Ir(Ⅲ) to Ir(Ⅳ) on the anode surface, which can be concluded into a reversible reaction as follows [23, 30]:

$$2IrO_2 + 2H+ + 2e- \leftrightarrow Ir_2O_3 + H_2O$$

As we know, the redox peak of the voltammetric curve is dependent on the structure and component of coating, dispersion of particle size, enlargement of active surface area, defects of the lattice, and even experimental conditions, etc [23, 24]. It is noted that the coating factor plays a more important role in its influence on the redox peak. Generally, it is thought the appearance of redox peak is arising from resultant fine IrO_2 crystals on the surface of the IrO_2/Ti anode, which causes its increase of the electrical contact improvement in the apparent electrochemical activity [31-33]. In this case, the nanowire array of IrO_2 coating significantly increases the specific surface

area of the activating oxide, which gives rise to higher opportunity to be oxidised and thus obtains an obvious redox peak as compared to the electrode with the substrate of densified Ti in Ref. [23].

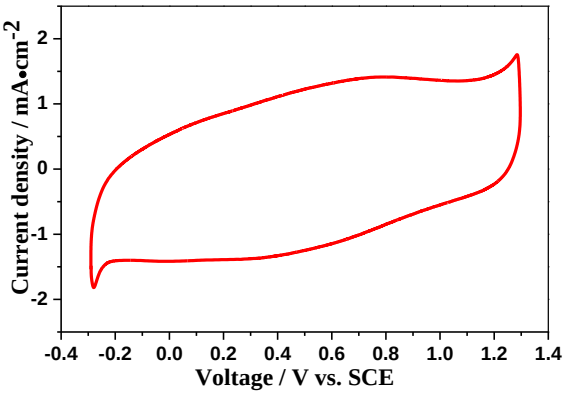

Fig. 11. Cyclic voltammograms of the Ti/IrO_2 anode at 40 mV/s in the electrolyte solution.

4. Conclusions

In this study, we fabricated large-scale porous Ti sheets using direct powder rolling followed by vacuum sintering. The microstructure either longitudinal or transverse to RD is homogenous. The porous Ti/IrO_2 electrode was successfully prepared by employing a brushing followed by thermal decomposition process. The following conclusions can be drawn from this study.

(1) The resultant microstructure and properties in terms of thickness, porosity, pore size, filtration and tensile properties are fairly uniform either longitudinal or transverse to RD.

(2) The specific surface area of the prepared IrO_2/Ti electrode is large attributed to the nanowire arrays on the electrode surface so that the reactivity of electrode improves.

(3) There occurred an obvious redox peak in the electrochemical test for the IrO_2/Ti electrode, dependent on the fine structure and component of the IrO_2 coating. The IrO_2/Ti electrode achieved more active surface area as compared to the result in other report.

Acknowledgement

We appreciate the funding from Shaanxi Science and Technology Co-ordination and Innovation Project (Nos. 2014KTZB01-02-04; 2014KTCQ 01-08).

5. References

1. C. Leyens and M. Peters: 'Titanium and titanium alloys: fundamentals and applications', 513; 2003, Wiley-VCH.
2. F. H. S. Froes: 'Titanium Alloys', in 'Handbook of Advanced Materials', (ed. K. James), 271; 2004, Wessel, Wiley Interscience.
3. D. Banerjee and J. C. Williams: 'Perspectives on Titanium Science and Technology', *Acta Materialia*, 2013, **61**(3), 844-879.
4. F. H. Froes Sam: '8 - Powder metallurgy of titanium alloys', in 'Advances in Powder Metallurgy', (eds. I. Chang, et al.), 202-240; 2013, Woodhead Publishing.
5. D. C. Dunand: 'Processing of titanium foams', *Advanced Engineering Materials*, 2004, **6**(6), 369-376.
6. G. Chen: 'Powder metallurgical titanium alloys (TiNi and Ti-6Al-4V): injection moulding, press-and-sinter, and hot pressing ', The University of Auckland New Zealand, 2014.
7. F. H. Froes and D. Eylon: 'Powder metallurgy of titanium alloys', *International Materials Reviews*, 1990, **35**(3), 162-184.
8. D. Eylon, F. H. Froes, and S. Abkowitz: 'Titanium Powder Metallurgy Alloys and Composites, ASM Handbook ', 1998, Materials Park, OH, Powder Metal Technologies and Applications, ASM International.
9. G. Vinogradov: 'Theory and Practice of Rolling Metal Powders', *Powder Metallurgy and Metal Ceramics*, 2002, **41**(9-10), 517-525.
10. T. A. Edison: 'Process for making thin metallic flakes', USA, Mar 2nd, 1909.
11. J. A. Roemer, B. H. Mckibben, and J. R. Corry: 'Method of rolling titanium sheets', USA, 1953.
12. G. M. D. Cantin, P. L. Kean, N. A. Stone, R. Wilson, M. A. Gibson, M. Yousuff, D. Ritchie, and R. Rajakumar: 'Innovative consolidation of titanium and titanium alloy powders by direct rolling', *Powder Metallurgy*, 2011, **54**(3), 188-192.
13. R. G. Vogt, D. Eylon, and F. H. Froes: 'Industrial applications of titanium and zirconium: Fourth volume', (eds. C. S. Young, et al.), 194-208; 1986, Philadelphia, PA, American Society for Testing and Materials.
14. R. F. Geisendorfer: 'Powder metallurgy of titanium alloys', (eds. F. H. Froes, et al.), 151-162; 1980, Warrendale, PA, Metallurgical Society of AIME.
15. D. Ro, M. Toaz, and V. Moxson: 'The Direct Powder-Rolling Process for Producing Thin Metal Strip', *JOM*, 1983, **35**(1), 34-39.
16. F. H. Froes and J. Pickens: 'Powder Metallurgy of Light Metal Alloys for Demanding Applications', *JOM*, 1984, **36**(1), 14-28.
17. V. Moxson, O. N. Senkov, and F. H. Froes: 'Innovations in titanium powder processing', *JOM*, 2000, **52**(5), 24-26.
18. G. Jackson and T. Fieldsend, USA, 1977.
19. V. S. Moxson and V. A. Duz: 'Process of direct powder rolling of blended elemental titanium alloys, titanium matrix composites, and titanium aluminides', USA, 2007.
20. D. Eylon and F. H. Froes, USA, 1990.
21. T. Nakagawa, N. S. Bjorge, and R. W. Murray: *J. Am. Chem. Soc.* , 2009, **131**, 15578-15579.

22. S. Sunde, I. A. Lervik, M. Tsypkin, and L. E. Owe: *Electrochim. Acta*, 2010, **55**, 7751-7760.
23. Y.-Y. Hou, J.-M. Hu, L. Liu, J.-Q. Zhang, and C.-N. Cao: 'Effect of calcination temperature on electrocatalytic activities of Ti/IrO2 electrodes in methanol aqueous solutions', *Electrochimica Acta*, 2006, **51**, 6258-6267.
24. J. Backholm, E. Avendano, A. Azens, G. d. M. Azevedo, E. Coronel, G. A. Niklassona, and C. G. Granqvist: 'Iridium-based oxides: Recent advances in coloration mechanism, structural and morphological characterization', *Solar Energy Materials & Solar Cells*, 2008, **92**, 91-96.
25. G. I. Aksenov: 'Theory of powder rolling. Part I', *Powder Metall Met Ceram*, 1970, **9**(5), 370-374.
26. G. I. Aksenov: 'Theory of powder rolling. Part II', *Powder Metall Met Ceram*, 1970, **9**(6), 456-460.
27. J. H. Tundermann and A. R. E. Singer: 'Deformation and densification during the rolling of metal powders', *Powder Metallurgy*, 1969, **12**(23), 219-242.
28. S. C. Deevi: 'Powder processing of FeAl sheets by roll compaction', *Intermetallics*, 2000, **8**, 679-685.
29. R. M. German: 'Powder Metallurgy Science', 1998, Princeton, Metal Powder Industries Federation.
30. M. Pourbaix: 'Atlas of Electrochemical Equilibria in Aqueous Solutions', 1966, Oxford, England, Pergamon Press.
31. F. Ye, J. Li, X. Wang, T. Wang, S. Li, H. Wei, Q. Li, and E. Christensen: 'Electrocatalytic properties of Ti/Pt–IrO2 anode for oxygen evolution in PEM water electrolysis', *International Journal of Hydrogen Energy*, 2010, **35**(15), 8049-8055.
32. A. Stoyanova, G. Borisov, E. Lefterova, and E. Slavcheva: 'Oxygen evolution on Ebonex-supported Pt-based binary compounds in PEM water electrolysis', *International Journal of Hydrogen Energy*, 2012, **37**(21), 16515-16521.
33. M. Carmo, D. L. Fritz, J. Mergel, and D. Stolten: 'A comprehensive review on PEM water electrolysis', *International Journal of Hydrogen Energy*, 2013, **38**(12), 4901-4934.